Hindawi
Advances in Materials Science and Engineering
Volume 2022, Article ID 6587934, 10 pages
https://doi.org/10.1155/2022/6587934

Research Article

Synthesis of Nickel Sulfide Thin Films and Nanocrystals from the Nickel Ethyl Xanthate Complex

Patience Adei Kotei,[1] **Nathaniel Owusu Boadi**,[1] **Selina Ama Saah**,[2] **and Michael Baah Mensah**[1]

[1]*Department of Chemistry, Kwame Nkrumah University of Science and Technology, Kumasi, Ghana*
[2]*Department of Chemical Sciences, University of Energy and Natural Resources, Sunyani, Ghana*

Correspondence should be addressed to Nathaniel Owusu Boadi; noboadi@gmail.com

Received 10 March 2022; Revised 31 May 2022; Accepted 7 July 2022; Published 30 July 2022

Academic Editor: Alessandro Martucci

Nickel sulfides have unique and diverse structural features, making them ideal for energy conversion and storage. This research focuses on the synthesis and characterization of nickel sulfide thin films and nanocrystals from nickel ethyl xanthate complex using spin-coating and solventless methods. The nickel ethyl xanthate complex ($C_6H_{10}S_4NiO_2$) was characterized using Fourier-transformed infrared (FT-IR), ultraviolet-visible (UV-Vis), and nuclear magnetic resonance (NMR) spectroscopies as well as thermogravimetric analysis (TGA). The NiS thin films and nanoparticles were analyzed with energy dispersive X-ray (EDX) spectroscopy and X-ray diffraction (XRD). Nickel ethyl xanthate was synthesized in an 81.2% yield. The bandgaps of the nickel sulfide obtained from the spin-coating method ranged from 4.35–4.88 eV. For the solventless method, the bandgap of the nickel sulfide ranged from 3.93–3.96 eV. The crystal phase observed from the spin-coating and solventless methods was α-NiS (hexagonal). A direct correlation was observed between annealing temperature, bandgap, and particle size.

1. Introduction

Colloidal synthetic approaches offer control of nanocrystal synthesis and a good yield [1]. Thermal decomposition is the most suitable approach to obtain monodispersed nanoparticles [2]. Thermal decomposition routes are quite economical and ensure uniformity in size, shape, chemical composition, and structural properties of nanocrystals [3]. This control is attained by varying and manipulating experimental conditions such as temperature, concentration, nucleation, and growth processes [4–6], as well as using metal or single-source precursors [7–10].

Single-source precursors minimize the use of pyrophoric and toxic reagents in the synthesis of materials [11, 12]. They are stable in air and moisture [13, 14] and offer a cleaner synthesis of nanoparticles and thin films [15].

Metal xanthate complexes constitute a class of single-source precursors with endearing properties [16]. They are usually stable in solution and can decompose at relatively low temperatures, usually below 200°C [12, 17, 18]. Manipulating their solubility and decomposition during a synthetic workup can be achieved by varying the length of the attached organic side chains [10, 19]. These complexes have been used to obtain metal chalcogenide nanoparticles and thin films [20–22].

Transition metal chalcogenides present remarkable alternatives for sustainable energy production and storage and have been investigated for use in solar cells, lithium-ion batteries, sensors, hydrogen evolution, transistors, and photocatalytic degradation [9, 23]. Transition metal sulfides are highly covalent and are generally classified into binary, ternary, and polynary metal sulfides based on the elemental composition of the complex [24]; Wang et al. [25]. Their physical, optoelectronic, and chemical properties are easily tunable owing to quantum confinement [26].

Nickel sulfide (NiS) is a vital transition metal sulfide due to its high electron conductivity, low-temperature processability, metal insulating behavior, and complex phase changes [27]. It has two polymorphs: α-NiS (hexagonal), which is stable at high temperatures (>379), and a rhombohedral β-NiS which is also stable at lower temperatures [28, 29]. NiS thin films and nanoparticles with varying stoichiometries (NiS, NiS_2, Ni_3S_2, Ni_3S_4, Ni_6S_5, Ni_7S_6, Ni_4S_{3+x}, $Ni_{3+x}S_2$, and Ni_9S_8) and nanostructures have been prepared using various starting materials and precursors [21, 30, 31]. Some methods used to synthesize nickel sulfide include thermal decomposition, hydrothermal treatment, and solvothermal methods [32, 33]. Comprehensive studies of the structural, morphological, catalytic, electrochemical, and optoelectronic properties of nickel sulfides have been reported [9, 34, 35]. Nickel sulfides have been used as toughening agents in glass, electrodes in batteries, catalytic material for hydrodenitrogenation, and hydrodesulphurization because of their low cost, easy availability, and good electron transport properties [10, 36]. However, research into obtaining monodispersed nanomaterials from single-source precursors is limited [9].

This study covers the synthesis and characterization of nickel ethyl xanthate (NiEtX) and discusses two routes to convert them to nickel sulfide thin films and nanocrystals. We also examine the properties of the obtained nickel sulfide.

2. Materials and Methods

Chloroform (99%), methanol (99.8%), toluene (99.9%), potassium ethyl xanthate (96%), and nickel chloride (96%) were procured from Sigma-Aldrich (U.S.A). The chemicals were used without further purification.

3. Instrumentation

UV–Vis absorption spectra for NiEtX precursors and NiS nanocrystals were obtained on a Shimadzu UVmini-1240 spectrophotometer using a quartz cuvette of 1 cm path length and toluene as the solvent and blank. The NiS thin films from the spin-coating method were placed on a stage in the spectrophotometer for absorbance measurements using air as the reference. The bare substrate (microscope glass slide) was used for run separately. Measurements were taken from 200 nm to 1000 nm in a 1-nm step. The bandgap energy of the films and nanocrystals was obtained from a Tauc plot.

The infrared spectrum of the NiEtX precursor was obtained on a Bruker Alpha FT-IR spectrometer (Platinum ATR). The samples were scanned as solids from $4000\,\mathrm{cm}^{-1}$–$400\,\mathrm{cm}^{-1}$. The different wavenumbers from the spectrum were compared to theoretical values to determine the different functional groups in the sample.

^{1}H (proton) and ^{13}C (carbon) NMR studies were carried out using a Bruker FT-NMR Avance 500 MHz spectrometer (Ettlingen, Germany). The sample was prepared by dissolving 10 mg of the synthesized nickel ethyl xanthate precursor in chloroform-d at room temperature. The chemical shifts and splitting patterns of the different hydrogen and carbon atoms present in the complex were compared to standard values in the literature.

The melting point of the precursor was determined using the Stuart SMP10 Scientific Melting Point Apparatus. A capillary tube was filled at one end with the sample and inserted into the melting point apparatus. The sample was monitored as it was heated. The temperatures at which the sample began to melt and completely melted were recorded.

The decomposition pathway and thermal properties of the nickel ethyl xanthate complex were ascertained with an SDT Q600 V20.9 Build 20 Thermogravimetric and Differential Scanning Calorimetry Analyzer (TGA-DSC). The sample was heated from 25°C to 600°C under a flow of nitrogen gas. The percentage change in weight and the percentage of the residue were compared to the theoretical decomposition of nickel sulfide in different xanthate precursors.

SEM-EDX analysis was carried out on a Phenom-World ProX Desktop scanning electron microscope coupled to a ProSuite EDX. The films and nanoparticles deposited on a glass substrate were carbon-coated using the Cressington Sputter Coater 108 Manual 6002, 6006 coating system before the analysis. The elemental composition of the films and nanoparticles was determined and quantified.

XRD analysis was performed with a PANalytical Empyrean diffractometer equipped with monochromated Cu-Kα radiation, using the K_alpha line at 1.54 angstroms (Å) and the K_beta line removed with a beta filter. The particle sizes for the nickel sulfide crystals and thin films prepared at the different annealing temperatures were calculated using the Scherrer equation. The peak pattern obtained from the XRD matched with NiS (ICDD number: 01-075-0613) ICDD PDF-4 database run on the HighScore software v.4.8.

4. Synthesis of Nickel Ethyl Xanthate (NiEtX)

Nickel chloride (1.05 g, 4.4 mmol) was dissolved with distilled water (33 mL) in a beaker. Potassium ethyl xanthate (2.64 g, 8.8 mmol) was dissolved with distilled water (66 mL) in another beaker. The potassium ethyl xanthate solution was added to the nickel chloride solution in a dropwise fashion. The mixture obtained was stirred continuously for three hours. The precipitate formed was then isolated by filtration. The precipitate/residue was washed with distilled water and dried. The solid obtained was dissolved in chloroform (10 mL) and recrystallized in methanol (200 mL). The crystals obtained were separated from the mother liquor by filtration. They were washed with excess methanol, followed by washing with excess water, and dried. The mass of the product was 1.08 g correlating to a percentage yield of 81.2%.

5. Synthesis of Nickel Sulfide (NiS) Thin Films

Nickel sulfide thin films were obtained from thermal decomposition (annealing) of the precursor on glass slides with sizes of 21 mm × 15 mm. The glass slides were cleaned by sonication in butanol and distilled water successively for 30 min before deposition. The precursor was dissolved in chloroform. A 50 mg/mL concentration was prepared and deposited on glass substrates by spin-coating (Ossila Spin

Coater) at 1200 rpm for 30 sec. Deposited precursor layers were converted to thin films by annealing in a preheated furnace (Carbolite-MTF 12/38/250) at 200°C for 30 min. The annealing temperature was then varied. This method was repeated for the annealing temperatures at 300°C and 400°C.

6. Synthesis of Nickel Sulfide (NiS) Nanocrystals

0.3 g of the nickel ethyl xanthate precursor was weighed into a ceramic boat lined with aluminum foil. The ceramic boat containing the NiEtX complex was placed at the center of a quartz tube and inserted into a preheated furnace (Carbolite-MTF 12/38/250). The sample was heated to the required temperature (200°C, 300°C, and 400°C) for 30 min. After the heating process, the furnace was allowed to cool. The product obtained (black powder) was collected and analyzed.

7. Results and Discussion

The nickel ethyl xanthate complex synthesized was obtained as dark-green crystals with a strong sulfur-like smell. The complex was stable and easy to handle. The percentage yield obtained was 81.2%. Compared to that obtained in the literature, the relatively lower yield could be attributed to mass loss during the purification step in chloroform and the successive recrystallization from chloroform using methanol [10, 37].

Xanthate ligands can coordinate with metal centers in monodentate, isobidentate, anisobidentate, or bridging modes [21]. The molecular structure of the complex is shown in Figure 1. The Ni (II) center assumes a square planar geometry. It is coordinated to four sulfur atoms from the ethyl xanthate ligand.

The observed melting point of the nickel ethyl xanthate precursor was relatively sharp, confirming the purity of the complex. The melting point obtained was 144°C–145°C, which conforms to reported values [21]. The theoretical melting point for potassium ethyl xanthate used for the initial synthesis is known to be 225°C–226°C. Generally, in contrast to the alkali metal salts of xanthates, heavy metal salts (e.g., Pb^{2+}, Cd^{2+}, and Ni^{2+}) of the same xanthates have lower melting points [38]. This could be the reason for low melting point obtained for the nickel ethyl xanthate. Their low melting point makes them suitable single-source precursors [22].

The nickel ethyl xanthate precursor was characterized using UV-Visible spectroscopy. As highlighted in Figure 2, the absorbance at 478 nm could be a d-d transition of the nickel (II) ion, and the absorbance at 416 nm could result from the metal-ligand charge transfer transitions. The two absorbance peaks were in the visible region of the electromagnetic spectrum, an indication that the complex is paramagnetic.

The FT-IR spectrum of NiEtX is presented in Figure 3. The observed stretching and vibration of bonds in NiEtX were in agreement with those previously reported on xanthates and nickel sulfide [9, 39]. The bands around 2980 cm^{-1} and 2978 cm^{-1} indicated the presence of the C–H functional group, which is attributed to the ethyl group. Distinctive vibrational bands of NiEtX at 1263 cm^{-1}, 1114 cm^{-1} and 1020 cm^{-1} were assigned to asymmetric C–O–C vibrations and C–S stretching, respectively [10]. The absorption bands at 434 cm^{-1}, 553 cm^{-1}, 659 cm^{-1}, 806 cm^{-1}, 859 cm^{-1}, and 993 cm^{-1} were associated with the Ni–S–Ni bending and vibration modes [32].

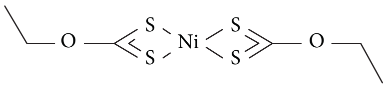

Figure 1: Molecular structure of the NiEtX complex.

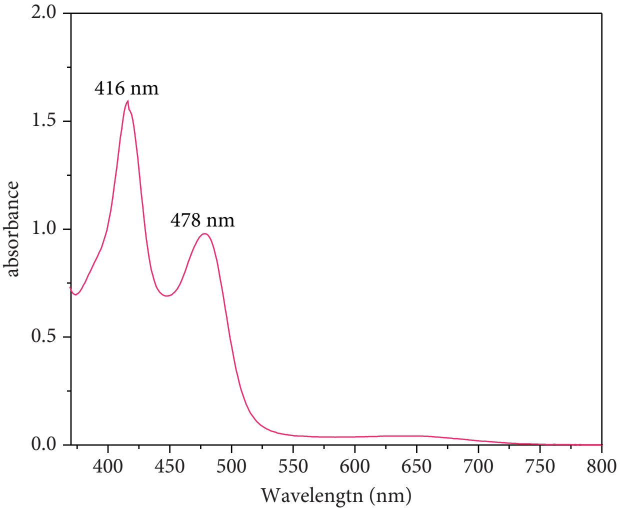

Figure 2: UV-Vis absorbance of the NiEtX complex.

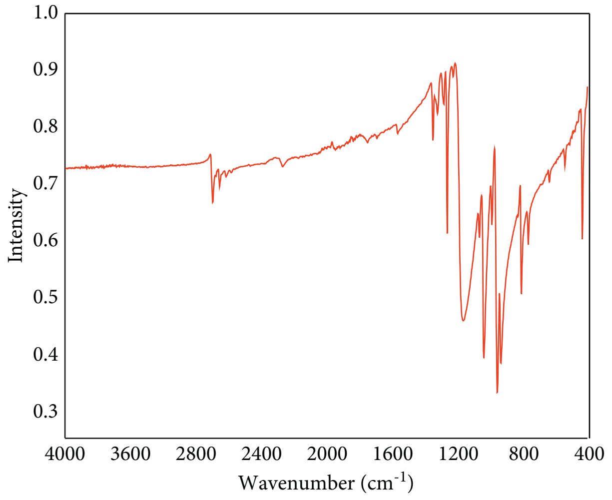

Figure 3: IR spectrum of the NiEtX complex.

The ^1H NMR spectrum of the NiEtX complex showed two distinct peaks with an integral of 1.5, as expected from the ethyl group. However, the splitting pattern was interfered by the paramagnetic nature of the nickel complex. The chemical shift (δ) for the methylene hydrogens was observed at 4.6 ppm. This downfield value (δ) resulted from the attachment of the carbon bearing the methylene hydrogens to a more electronegative oxygen atom. The chemical shift for the methyl hydrogens were observed at 1.5 ppm (Table 1).

The ^{13}C NMR showed two peaks at 17.2 ppm (CH_3) and 69.6 ppm (CH_2) as indicated in Table 1. The signal from the quaternary carbon was not observed. It may be due to the paramagnetic nature of the Ni (II) metal and the presence of unpaired electrons in the complex [40]. These factors could interact with the applied magnetic field and spin resonance which further interrupts the relaxation time of the excited nuclei.

Thermal analysis of NiEtX [Ni $(C_2H_5OCS_2)_2$] was performed between a temperature range of 25–600°C. A single step decomposition was identified for NiEtX with a steep weight loss of 46.61% between 155°C–200°C (Figure 4). The onset and endset temperatures were 169.1 and 212°C, respectively. The expected weight loss was 38.20%, in contrast to the observed 46.61%. This could be attributed to the complex phase transition and inversion of nickel sulfides on heating [41]. However, some residue decomposition and uncertainties in the thermogravimetric measurement setup might have also contributed to this variation [10]. The percentage weight loss from the TGA is indicative of the formation of NiS in the residue obtained.

The spin-coating and solventless methods were used to deposit and prepare NiS thin films and nanoparticles, respectively. For each method, the annealing temperatures were varied to estimate how temperature affects the morphology and properties of NiS. Films of NiS were obtained using the spin-coating method. Bandgaps of NiS deposited at the different annealing temperatures were ascertained using Tauc plots obtained from their UV-Visible spectra.

Figure 5 shows the absorbance spectra and Tauc plots of NiS using spin-coating and solventless methods. The NiS absorbed significantly in the UV region and very low in the visible region. The estimated bandgap energy of NiS from the spin-coating method ranged from 4.35–4.88 eV and 3.93–3.96 eV from the solventless method. A significant blue shift was observed in comparing the values obtained to the bandgap energy of bulk NiS which is ~2.1 eV [36]. The bandgap decreased with increasing temperature. This observation could be attributed to the agglomeration of the particles with increasing temperature, with a corresponding decrease in the bandgap. The NiS obtained from both methods can find wide applications in energy conversion, energy storage, and catalysis based on their bandgaps. The bandgap values obtained for the NiS nanoparticles were lower than the thin films obtained from the spin-coating method. This could be due to variations in the kind of particles produced and their size effects [36].

8. Morphological Characterization

The morphology and orientation of the particles in both the thin films and nanocrystals can be affected by the synthetic method, temperature and substrate used for deposition.

Table 1: ^{1}H and ^{13}C NMR of the nickel ethyl xanthate (NiEtX) complex.

Atoms	δ/ppm (^{1}H)	δ/ppm (^{13}C)
CH_2	4.6	69.6
CH_3	1.5	17.2

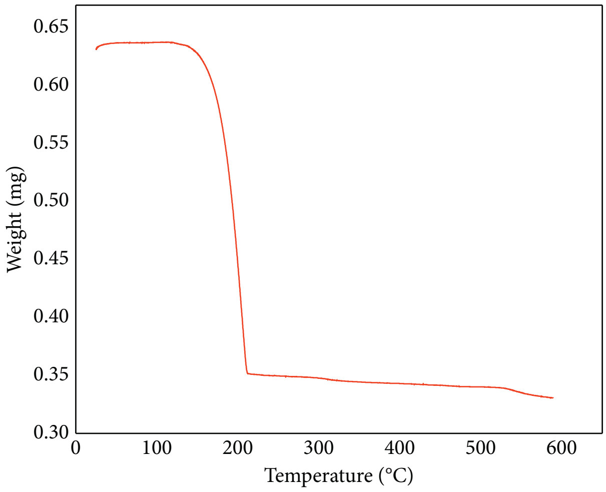

Figure 4: TGA curve of the NiEtX complex. Characterization of nickel sulfate (NiS) thin films and nanocrystals.

EDX was used to detect and quantify the elemental composition of the thin films and nanocrystals prepared. The elemental composition of the NiS obtained from the decomposition of nickel ethyl xanthate comprised of Ni and S atoms. Table 2 shows the atomic concentrations obtained for the thin films and nanocrystals at different temperatures. The stoichiometry of Ni to S was comparable to those reported [9, 31, 32]. The atomic composition of sulfur decreased as temperature increased, possibly because of the volatile nature of the sulfur at higher temperatures [41].

9. Structural and Particle Size Characterization

9.1. XRD Analysis. XRD patterns of the thin films and nanocrystals prepared from NiEtX are shown in Figures 6 and 7, respectively. A crystalline hexagonal (α-NiS) phase was attained (ICDD # 01-075-0613) for both the spin-coating and solventless methods. The diffraction pattern for the spin-coating method showed low-intensity peaks for the α-NiS phase. Particle sizes obtained from the Scherrer equation for the spin-coating method at 200°C, 300°C, and 400°C were 19 nm, 22 nm, and 27 nm, respectively. The large peak widths seen confirmed the small sizes obtained for the particles. The most preferred orientation for the spin-coating approach was observed along the (1 0 2) plane.

The diffraction patterns for the solventless method showed high α-NiS phase intensity peaks with particle sizes of 20 nm, 21 nm, and 22 nm, respectively, at 200°C, 300°C, and 400°C. There was a steady increase in size with a corresponding temperature rise. This is expected [42] as the agglomeration of nanocrystals occurs with increasing

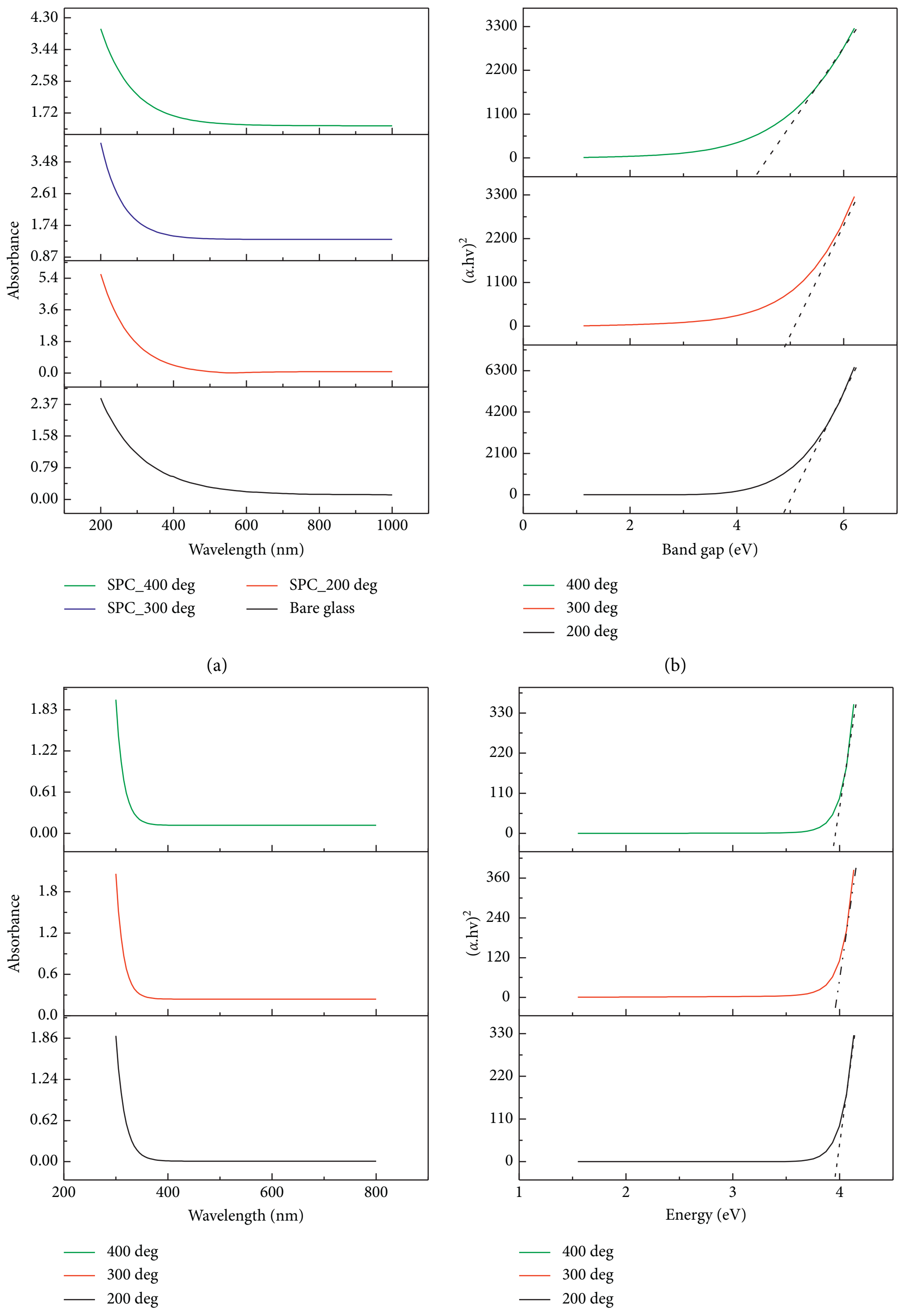

(a) (b)

(c) (d)

Figure 5: Absorption spectra for NiS produced from spin-coating (a) and solventless (c) methods and stacked Tauc plots showing bandgap energies of NiS from the spin-coating (b) and solventless (d) methods at 200°C, 300°C, and 400°C.

temperature. The preferred orientation was also observed along the (1 0 2) plane.

Williamson-Hall size and strain analysis plot was employed in the studies of the individual contribution of the lattice strain on crystallite sizes to the peak broadening observed in the diffraction pattern (Figure 8). Peak broadening could result from the existence of residual strain and line defects. Perfect crystals extend infinitely in all

Table 2: EDX of NiS thin films and nanocrystals at 200°C, 300°C, and 400°C.

Temperature	Element symbol	Atomic concentration (%)/SPC	Atomic concentration (%)/solventless
(a) 200°C	Ni	54.55	57.33
	S	45.45	42.67
(b) 300°C	Ni	54.48	58.39
	S	45.53	41.61
(c) 400°C	Ni	61.64	60.52
	S	38.36	39.58

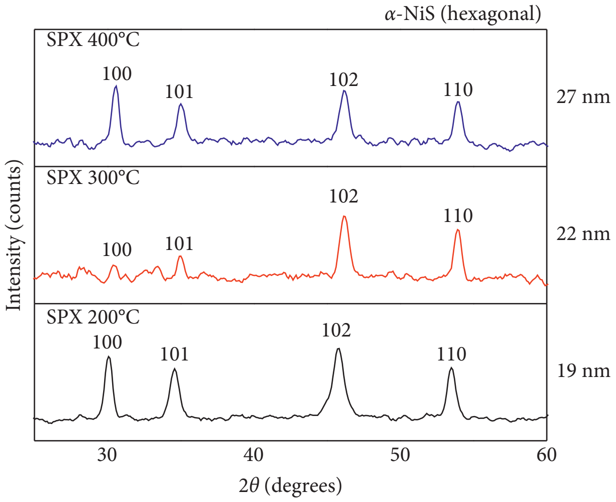

Figure 6: XRD patterns of NiS thin films obtained from the spin-coating method at 200°C, 300°C, and 400°C (crystallite sizes are shown on the side).

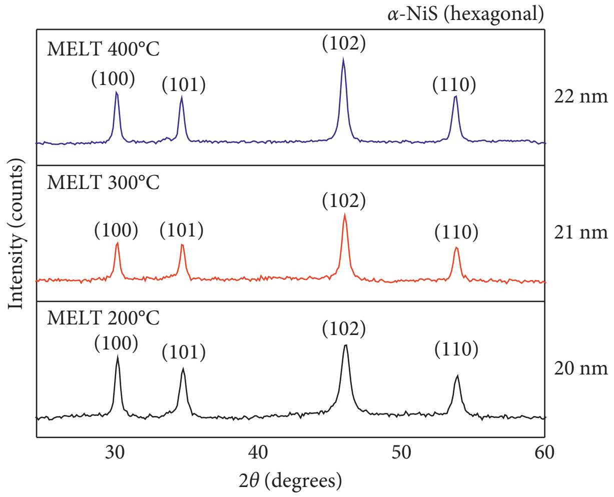

Figure 7: XRD patterns of NiS nanocrystals obtained from the solventless method at 200°C, 300°C, and 400°C (crystallite sizes are shown on the side).

directions [43]. Thus, the crystals obtained were imperfect due to their finite size. This deviation from perfection leads to the broadening of diffraction peaks [44]. The negative intercepts obtained from some of the W-H plots could be attributed to the compressive nature of the microstrain [45]. Table 3 shows the lattice strain and crystallite sizes obtained for particles from the spin-coating and solventless methods. The crystallite size calculated from the FWHM ranged from 3.1 to 9.734 nm for the spin-coating method and from 27.4 nm to 96.43 nm for the solventless method. The strain increased as the crystallite size decreased due to the lattice shrinkage effect. The improvement in the crystallinity of NiS nanoparticles from the solventless method is directly related to the increase in the grain size [46].

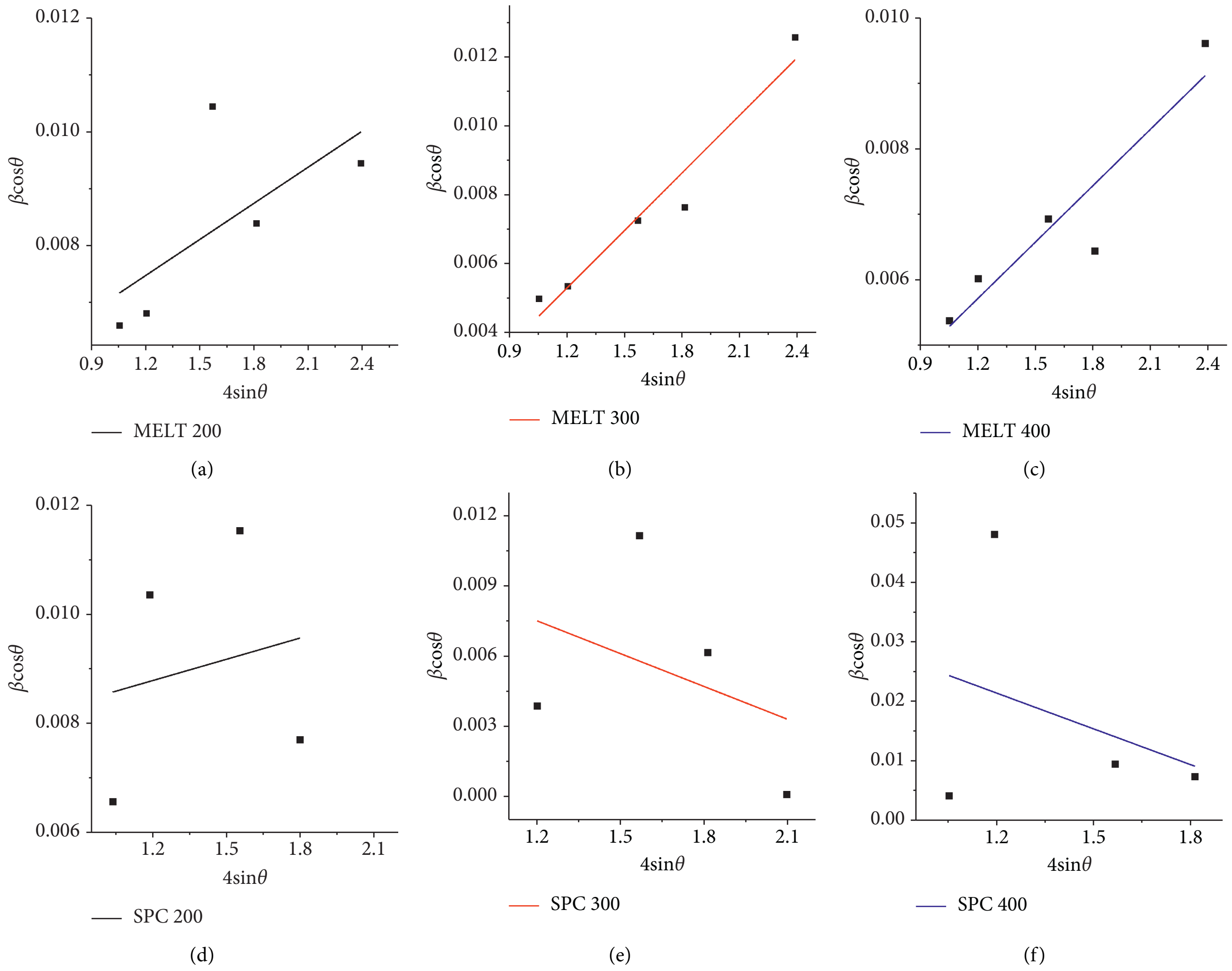

(a) (b) (c)

(d) (e) (f)

Figure 8: W-H plot analysis of NiS films obtained by spin-coating and nanoparticles obtained from the solventless method.

Table 3: Crystallite size and strain of NiS films obtained by spin-coating and nanocrystals obtained from the solventless method at 200°C, 300°C, and 400°C.

Temperature	Parameter	Spin coating	Solventless
(a) 200°C	Crystallite size	9.49 nm	27.4 nm
	Strain	−0.00425	0.00212
(b) 300°C	Crystallite size	10.5 nm	96.43 nm
	Strain	−0.00469	0.00557
(c) 400°C	Crystallite size	3.1 nm	59.73 nm
	Strain	−0.02004	0.00287

Dislocation densities (δ) and microstrains (ε) developed in thin films and nanoparticles were calculated. It was perceived that their dislocation densities and microstrains decline with an increase in crystallite sizes, as presented in Figures 9 and 10. This inverse relationship points toward fewer lattice imperfections [47]. This reflects the decrease in grain boundaries as the crystallite size in thin films and nanoparticles increases with temperature.

Some studies have significantly highlighted the effects of synthetic method variation and manipulation of preparation conditions on the characteristics of the product obtained [5, 48]. The size variation observed with temperature change could account for the difference in the bandgap values obtained [14]. Although the solventless method produced large grain sizes, the crystallite size obtained was smaller compared to that of the spin-coating method. Generally, large bandgap values are obtained from smaller crystals due to quantum confinement [49]. This assertion could explain the large bandgap values obtained from the solventless method.

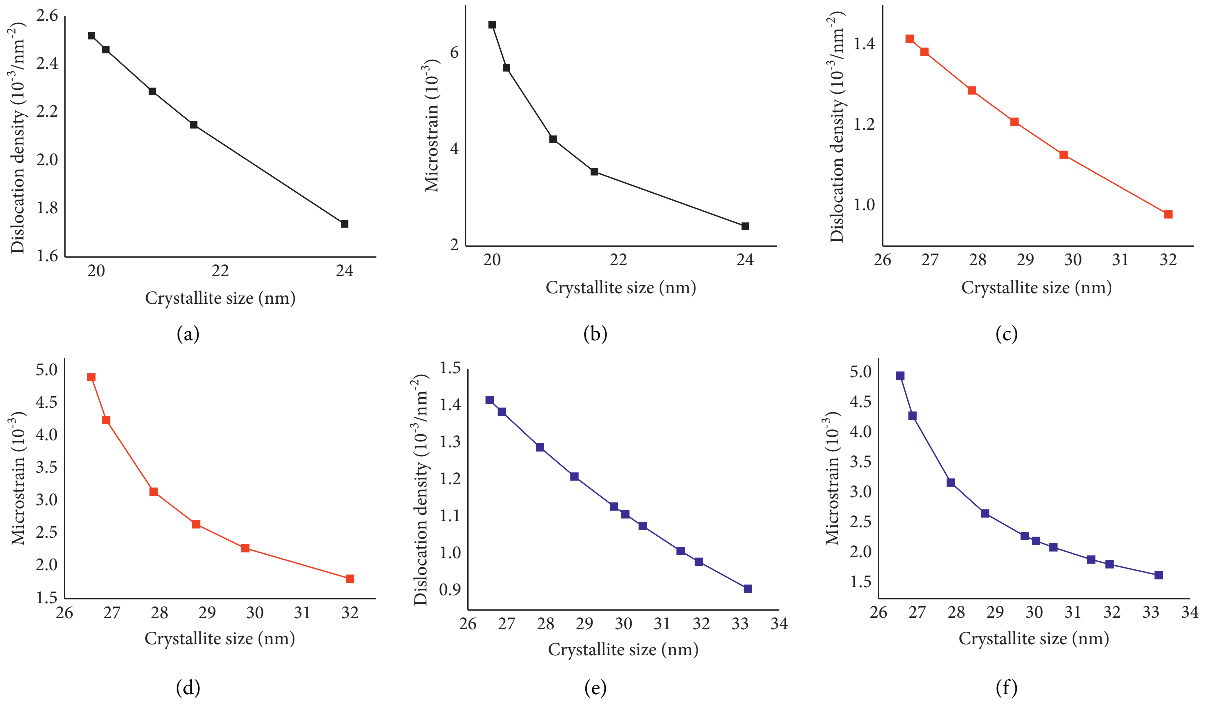

(a) (b) (c)

(d) (e) (f)

FIGURE 9: Variation of dislocation density and microstrain with crystallite size of NiS nanoparticles obtained from the solventless method at 200°C, 300°C, and 400°C.

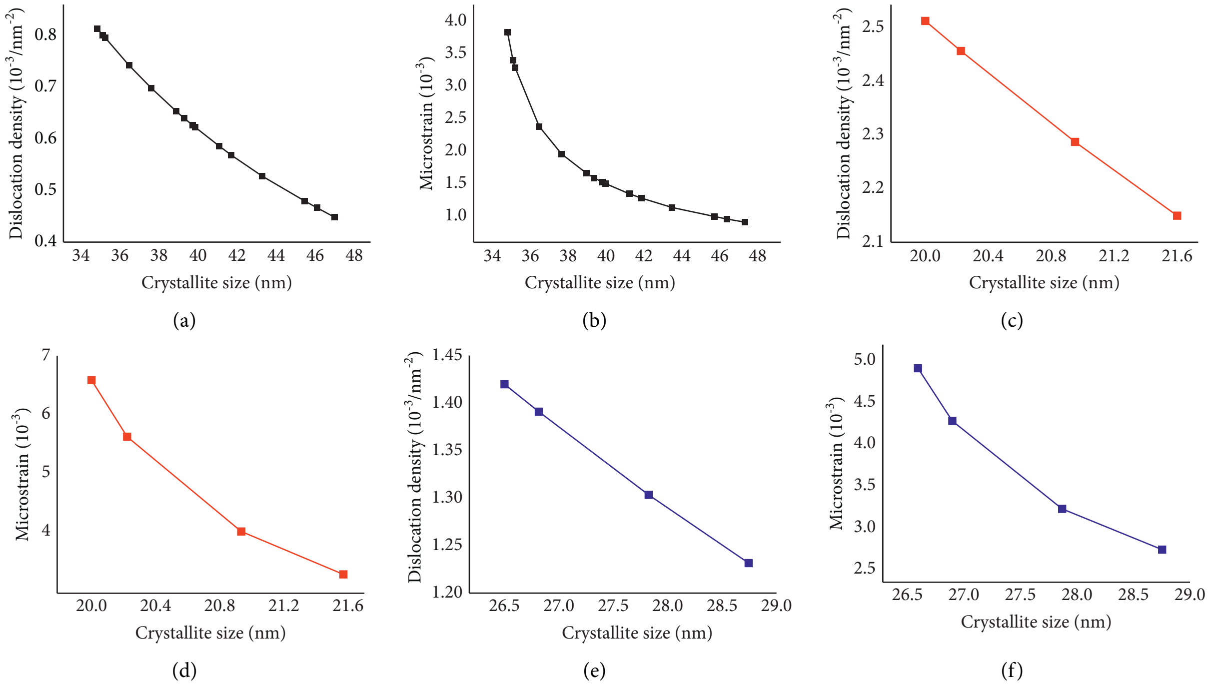

(a) (b) (c)

(d) (e) (f)

FIGURE 10: Variation of dislocation density and microstrain with the crystallite size of NiS thin films obtained by spin-coating at 200°C, 300°C, and 400°C.

10. Conclusions

Nickel ethyl xanthate ($C_6H_{10}S_4NiO_2$) was synthesized and characterized. As per its desirable potential in the preparation and deposition of NiS thin films and nanoparticles, its structure was analyzed using UV-Vis, NMR, and FT-IR spectroscopies. Additionally, thermogravimetric analysis was used to study its thermal behavior and decomposition pathway. The thermal analysis disclosed the prospect of obtaining NiS by thermal decomposition of the nickel ethyl xanthate precursor below 400°C. From the XRD analysis, all the thin films and nanoparticles indicated the growth of α-NiS (hexagonal) regardless of the annealing temperature. The spin-coating method for synthesizing NiS thin films from nickel ethyl xanthate was proved effective since the EDX analysis confirmed the presence of nickel and sulfur. Also, monodispersed NiS nanoparticles were obtained from the solventless method at 200°C. [50, 51].

Data Availability

Supplementary data will be available from the corresponding author upon request.

Conflicts of Interest

The authors declare that they have no conflicts of interest.

Acknowledgments

The authors would like to thank the Department of Chemistry of the Kwame Nkrumah University of Science and Technology, Kumasi for providing the laboratory facilities for this research.

References

[1] T. Palacios-Hernández, G. A. Hirata-Flores, O. E. Contreras-López et al., “Synthesis of Cu and Co metal oxide nanoparticles from thermal decomposition of tartrate complexes,” *Inorganica Chimica Acta*, vol. 392, pp. 277–282, 2012.

[2] A. T. Odularu, “Metal nanoparticles: thermal decomposition, biomedicinal applications to cancer treatment, and future perspectives,” *Bioinorganic Chemistry and Applications*, Hindawi Limited, vol. 2018, pp. 1–6, Hindawi Limited , 2018.

[3] R. Hufschmid, H. Arami, R. M. Ferguson et al., “Synthesis of phase-pure and monodisperse iron oxide nanoparticles by thermal decomposition,” *Nanoscale*, Royal Society of Chemistry, vol. 7, no. 25, pp. 11142–11154, 2015.

[4] F. Aslan, G. Adam, P. Stadler, A. Goktas, I. H. Mutlu, and N. S. Sariciftci, “Sol-gel derived in 2 S 3 buffer layers for inverted organic photovoltaic cells,” *Solar Energy*, Elsevier, vol. 108, , pp. 230–237, 2014.

[5] A. Goktas, S. Modanlı, A. Tumbul, and A. Kilic, “Facile synthesis and characterization of ZnO, ZnO:Co, and ZnO/ZnO:Co nano rod-like homojunction thin films: role of crystallite/grain size and microstrain in photocatalytic performance,” *Journal of Alloys and Compounds*, Elsevier, vol. 893, , Article ID 162334, 2022.

[6] S. Goktas and A. Goktas, “A comparative study on recent progress in efficient ZnO based nanocomposite and heterojunction photocatalysts: a review,” *Journal of Alloys and Compounds*, Elsevier, vol. 863, , 2021.

[7] F. Kirner, P. Potapov, J. Schultz et al., “Additive-controlled synthesis of monodisperse single crystalline gold nanoparticles: interplay of shape and surface plasmon resonance,” *Journal of Materials Chemistry C*, vol. 8, no. 31, pp. 10844–10851, 2020.

[8] A. Lassenberger, T. A. Grünewald, P. D. J. van Oostrum et al., “Monodisperse iron oxide nanoparticles by thermal decomposition: elucidating particle formation by second-resolved in situ small-angle X-ray scattering,” *Chemistry of Materials*, vol. 29, no. 10, pp. 4511–4522, 2017.

[9] G. B. Shombe, M. D. Khan, C. Zequine, C. Zhao, R. K. Gupta, and N. Revaprasadu, “Direct solvent free synthesis of bare α-NiS, β-NiS and α-β-NiS composite as excellent electrocatalysts: e,” *Scientific Reports*, Springer US, vol. 10, no. 1, pp. 1–14, 2020.

[10] A. Torvisco, P. Poelt, K. Wewerka et al., “Materials Nickel Sulfide Thin Films and Nanocrystals Synthesized from Nickel Xanthate Precursors”,” *Journal of Materials Science*, vol. 52, pp. 10898–10914, 2017.

[11] N. O. Boadi, S. A. Saah, and J. A. M. Awudza, “Synthesis of a novel single-source precursor for the production of lead chalcogenide thin films,” *Journal of Chemistry*, vol. 2020, pp. 1–7, 2020a.

[12] S. A. Saah, N. O. Boadi, D. Adu-Poku, and C. Wilkins, “Lead ethyl dithiocarbamates: efficient single-source precursors to PbS nanocubes,” *Royal Society Open Science*, vol. 6, no. 190943, pp. 1–8, 2019a.

[13] N. O. Boadi, S. A. Saah, M. B. Mensah, and J. A. M. Awudza, “Aerosol-Assisted chemical vapour deposition of lead chalcogenide thin films from [Pb((SePiPr2)2N)(S2CNHexMe)],” *Advances in Materials Science and Engineering*, vol. 2020, pp. 1–7, 2020b.

[14] S. A. Saah, N. O. Boadi, and C. Wilkins, “Deposition of PbS thin films from lead hexadecyl and octadecyl xanthate complexes using the spin coating method,” *MRS Advances*, vol. 4, no. 11-12, pp. 733–742, 2019b.

[15] A. Ali, H. Zafar, M. Zia et al., “Synthesis, characterization, applications, and challenges of iron oxide nanoparticles,” *Nanotechnology, Science and Applications*, vol. 9, pp. 49–67, 2016.

[16] M. A. Malik, N. Revaprasadu, and P. O’Brien, “Air-stable single-source precursors for the synthesis of chalcogenide semiconductor nanoparticles,” *Chemistry of Materials*, vol. 13, no. 3, pp. 913–920, 2001.

[17] N. O. Boadi, M. A. Malik, P. O’Brien, and J. A. M. Awudza, *Single source molecular precursor routes to lead chalcogenides*, vol. 41, no. 35, pp. 10497–10506, Cambridge, England, Dalton Transactions, 2012.

[18] M. A. Elizondo-Álvarez, A. Uribe-Salas, and S. Bello-Teodoro, “Chemical stability of xanthates, dithiophosphinates and hydroxamic acids in aqueous solutions and their environmental implications,” *Ecotoxicology and Environmental Safety*, vol. 207, Academic Press, Article ID 111509, 2021.

[19] Y. Shen, D. R. Nagaraj, R. Farinato, and P. Somasundaran, “Study of xanthate decomposition in aqueous solutions,” *Minerals Engineering*, vol. 93, pp. 10–15, Elsevier, 2016.

[20] J. X. Liang, H. J. Zhong, G. Yang, K. Vellaisamy, D. L. Ma, and C. H. Leung, “Recent development of transition metal complexes with in vivo antitumor activity,” *Journal of Inorganic Biochemistry*, vol. 177, Elsevier, 2017.

[21] A. M. Qadir, “Synthesis, characterization and antibacterial activities of two nickel(II) complexes with xanthate derivatives and N,N,N′,N′-tetramethylethylenediamine as ligands,” *Transition Metal Chemistry*, vol. 42, no. 1, pp. 35–39, Springer International Publishing, 2017.

[22] J. Takaya and J. Takaya, “Catalysis using transition metal complexes featuring main group metal and metalloid compounds as supporting ligands,” *Chemical Science*, Royal Society of Chemistry, February, 2021.

[23] Q. Wang, J. Huang, H. Sun, Y. H. Ng, K. Q. Zhang, and Y. Lai, “MoS2 quantum dots@TiO2 nanotube Arrays: an extended-spectrum-driven photocatalyst for solar hydrogen evolution,” *ChemSusChem*, vol. 11, no. 10, pp. 1708–1721, 2018.

[24] S. Chandrasekaran, L. Yao, L. Deng et al., "Recent advances in metal sulfides: from controlled fabrication to electrocatalytic, photocatalytic and photoelectrochemical water splitting and beyond," *Chemical Society Reviews*, vol. 48, pp. 4178–4280, 2019.

[25] J. Wang, S. Lin, N. Tian, T. Ma, Y. Zhang, and H. Huang, "Nanostructured metal sulfides: classification, modification strategy, and Solar-Driven CO2 reduction application," *Advanced Functional Materials, Wiley-VCH Verlag*, vol. 31, no. 9, p. 2008008, 2019.

[26] A. L. Robbert, M. Donald, K. Yu et al., "Low-temperature noninjection approach to homogeneously-alloyed PbSexS1 − x colloidal nanocrystals for photovoltaic applications," *Applied Materials and Interfaces*, vol. 3, no. 5, pp. 1511–1520, 2011.

[27] S. Surendran, K. V. Vijaya Sankar, L. J. John Berchmans, and R. K. Kalai Selvan, "Polyol synthesis of α-NiS particles and its physico-chemical properties," in *Materials Science in Semiconductor Processing*, vol. 33, pp. 16–23, Elsevier, 2015.

[28] D. W. Bishop, P. S. Thomas, and A. S. Ray, "Raman spectra of nickel(II) sulfide," *Materials Research Bulletin*, Elsevier, vol. 33, no. 9, pp. 1303–1306, 1998.

[29] L. Wang, Y. Zhu, H. Li, Q. Li, and Y. Qian, "Hydrothermal synthesis of NiS nanobelts and NiS2 microspheres constructed of cuboids architectures," *Journal of Solid State Chemistry*, Academic Press, vol. 183, no. 1, pp. 223–227, 2010.

[30] F. K. A. Jarah and S. E. Al, "Preparation and characterization of some transition metal complexes with OleylXanthate and 1,10- phenanthrolin," *Rafidain Journal of Science*, University of Mosul, vol. 28, no. 2, pp. 228–234, 2019.

[31] A. Molla, M. Sahu, and S. Hussain, "Scientific reports," *Synthesis of Tunable Band Gap Semiconductor Nickel Sulphide Nanoparticles: Rapid and Round the Clock Degradation of Organic Dyes"*, Nature Publishing Group, vol. 6, pp. 1–11, 2016.

[32] Y. Fazli, S. M. Pourmortazavi, I. Kohsari, and M. Sadeghpur, "Electrochemical synthesis and structure characterization of nickel sulfide nanoparticles," *Materials Science in Semiconductor Processing*, Elsevier, vol. 27, no. 1, pp. 362–367, 2014.

[33] C. Z. Kang, F. S. Omar, S. Gunalan, K. Ramesh, and S. Ramesh, "Coral-like structured nickel sulfide-cobalt sulfide binder-free electrode for supercapattery," *Ionics*, vol. 26, no. 7, pp. 3621–3630, 2020.

[34] A. Roffey, N. Hollingsworth, H. U. IslamIslam et al., "Phase control during the synthesis of nickel sulfide nanoparticles from dithiocarbamate precursors," *Nanoscale*, vol. 8, no. 21, pp. 11067–11075, 2016.

[35] C. S. Thangwane, T. Xaba, and M. J. Moloto, "the formation of the mixed morphology of nickel sulfide nanoparticles derived from substituted benzimidazole dithiocarbamate nickel (ii) complexes," *Chalcogenide Letters*, vol. 14, no. 9, pp. 407–417, 2017.

[36] M. Kristl, B. Dojer, S. Gyergyek, and J. Kristl, "Synthesis of nickel and cobalt sulfide nanoparticles using a low cost sonochemical method," *Heliyon*, vol. 3, no. 3, Article ID e00273, 2017.

[37] P. L. Musetha, N. Revaprasadu, M. A. Malik, and P. O'Brien, "The use of xanthates as precursors for the deposition of nickel sulfide thin films by aerosol assisted chemical vapour deposition," *MRS Proceedings*, vol. 879, p. Z7.4, 2005.

[38] G. H. Harris, "Xanthates," *Kirk-Othmer Encyclopedia of Chemical Technology*, John Wiley & Sons, Hoboken, New Jersey, 2000.

[39] M. Akhtar, N. Revaprasadu, M. A. Malik, and J. Raftery, "Deposition of phase pure nickel sulfide thin films from bis(O-alkylxanthato)-nickel(II) complexes by the aerosol assisted chemical vapour deposition (AACVD) method," *Materials Science in Semiconductor Processing*, vol. 30, pp. 368–375, Elsevier, 2015.

[40] C. Schaller, *UV-visible Spectroscopy - Metal Ions"*, https://chem.libretexts.org/@go/page/189755, 2020.

[41] G. Kullerud and R. A. Yund, "The Ni-S system and related minerals," *Journal of Petrology*, vol. 3, no. 1, pp. 126–175, 1962.

[42] J. M. Clark, G. Kociok-Köhn, N. J. Harnett et al., "Formation of PbS materials from lead xanthate precursors," *Dalton Transactions*, vol. 40, no. 26, p. 6893, 2011.

[43] V. Mote, Y. Purushotham, and B. Dole, "Williamson-Hall analysis in estimation of lattice strain in nanometer-sized ZnO particles," *Journal of Theoretical and Applied Physics*, vol. 6, no. 1, p. 6, 2012.

[44] A. K. Zak, M. E. Abrishami, and R. Yousefi, "X-ray analysis of ZnO nanoparticles by Williamson-Hall and size-strain plot methods," *Solid State Sciences*, Elsevier Masson, vol. 13, no. 1, pp. 251–256, 2011.

[45] B. Yahmadi, N. Kamoun, C. Guasch, and R. Bennaceur, "Synthesis and characterization of nanocrystallized In2S 3 thin films via CBD technique," *Materials Chemistry and Physics*, Elsevier B.V, vol. 127, no. 1–2, pp. 239–247, 2011.

[46] R. Romero, F. Martin, J. R. Barrado, and D. Leinen, "Synthesis and characterization of nanostructured nickel oxide thin films prepared with chemical spray pyrolysis," *Thin Solid Films*, vol. 518, no. 16, pp. 4499–4502, 2010.

[47] A. Begum, A. Hussain, and A. Rahman, "Effect of Deposition Temperature on the Structural and Optical Properties of Chemically Prepared Nanocrystalline lead Selenide Thin Films," *Beilstein Journal of Nanotechnology*, vol. 3, pp. 438–43, June 2012.

[48] A. Goktas, "Sol-gel derived Zn1−xFexS diluted magnetic semiconductor thin films: c," *Applied Surface Science*, vol. 340, pp. 151–159, Elsevier B.V, 2015.

[49] T. Edvinsson, "Optical quantum confinement and photocatalytic properties in two-, one- and zerodimensional nanostructures," *Royal Society Open Science, Royal Society Publishing*, vol. 5, no. 9, 2018.

[50] A. Ghezelbash, M. B. Sigman, and B. A. Korgel, "Solventless synthesis of nickel sulfide nanorods and triangular nanoprisms," *Nano Letters*, vol. 4, no. 4, pp. 537–542, 2004.

[51] C. Sun, M. Ma, J. Yang et al., "Phase-controlled synthesis of α-NiS nanoparticles confined in carbon nanorods for High Performance Supercapacitors," *Scientific Reports*, vol. 4, no. 1, p. 7054, 2014.